Title
Time-resolved emission and scattering imaging of plume dynamics and nanoparticle ejection in femtosecond laser ablation of silver thin films

Journal
Applied Physics Letters, 116(23)

ISSN
0003-6951

Authors
Park, Minok
Jeun, Jinhong
Han, Gyoowan
et al.

Publication Date
2020-06-08

DOI
10.1063/5.0009227

Peer reviewed

Applied Physics Letters

Time-resolved emission and scattering imaging of plume dynamics and nanoparticle ejection in femtosecond laser ablation of silver thin films

Cite as: Appl. Phys. Lett. **116**, 234105 (2020); https://doi.org/10.1063/5.0009227
Submitted: 30 March 2020 . Accepted: 29 May 2020 . Published Online: 09 June 2020

Minok Park, Jinhong Jeun, Gyoowan Han, and Costas P. Grigoropoulos

Applied Physics Letters ARTICLE scitation.org/journal/apl

Time-resolved emission and scattering imaging of plume dynamics and nanoparticle ejection in femtosecond laser ablation of silver thin films

Cite as: Appl. Phys. Lett. **116**, 234105 (2020); doi: 10.1063/5.0009227
Submitted: 30 March 2020 · Accepted: 29 May 2020 ·
Published Online: 9 June 2020

View Online Export Citation CrossMark

Minok Park,[1] Jinhong Jeun,[2] Gyoowan Han,[2] and Costas P. Grigoropoulos[1,a)]

AFFILIATIONS

[1]Laser Thermal Laboratory, Department of Mechanical Engineering, University of California, Berkeley, California 94720-1740, USA
[2]Samsung Display, 1 Samsung-ro, Giheung-gu, Yongin-si, Gyeonggi-do 17113, South Korea

[a)]**Author to whom correspondence should be addressed:** cgrigoro@berkeley.edu. **Tel.:** +1 510 642 2525. **Fax:** +1 510 642 5539

ABSTRACT

Time-resolved emission and scattering imaging are employed to analyze the ablation mechanisms of silver thin films induced by femtosecond laser irradiation of Gaussian intensity profile under different laser fluences and gas background pressures. At fluences near the ablation threshold, nanoparticles (NPs) of 40 nm–100 nm in size are ejected in the vertical direction from the target sample. The average ejection speed of these NPs increases with the laser fluence and also as the background gas pressure drops from ambient atmospheric to $\sim 10^{-5}$ Torr. At higher fluences, a plume is formed at the center of the laser beam and NPs are released in oblique trajectories from the peripheral area of the laser-irradiated spot.

Direct laser ablation for patterning metal thin films has been implemented in optoelectronic applications because it can accomplish one-step fabrication, thereby reducing the number and complexity of processing procedures compared to conventional photolithography methods.[1,2] Of particular interest is the ultrafast femtosecond laser that offers the ability to produce well-defined ablated features. In this case, the energy deposition time (~100 fs) is shorter than the electron-phonon relaxation time (~10 ps for metals) and detrimental thermal damage can be avoided.[3] Fundamental understanding of ablative material removal dynamics by the femtosecond laser is essential for achieving high-quality ablated patterns, enabling advanced applications that may require fabrication of submicron craters,[4] minimized burr size,[5] and nanostructures.[6,7]

Above the plasma formation threshold, ablation dynamics induced by the femtosecond laser have been characterized by emission and the associated laser-induced breakdown spectroscopic techniques.[4,8,9] On the other hand, ablation of metal thin films entails the formation of nanoparticles (NPs), either from hydrodynamic instability of the molten pool or via spallation and phase explosion as predicted by molecular dynamics simulations.[10,11]

Several attempts have been made to experimentally probe dynamics of generated NPs. NPs could be detected by continuum emission from blackbody radiation at certain time delays.[12,13] However, the entire ablation process cannot be examined by emission imaging because of the rapid expansion and cooling. Time-resolved shadowgraph imaging has been utilized to visualize the dynamics of excimer laser-induced forward transfer (LIFT), but it is difficult for this method to resolve NPs that present low extinction cross sections. Accordingly, sufficient number density of ablated particles is required, but this condition is elusive in the case of thin films. Comprehensive analysis of the entire ablation process, including the ejection of plasma plume and NPs by the femtosecond laser, should be conducted.

In this Letter, to elucidate the ablation mechanisms of silver thin films, we investigate the plume evolution by gated emission imaging and the dynamics of NPs by scattering probing via an Ar^+ laser, under different pressure conditions of 760 Torr and 10^{-5} Torr. The scattering probing can capture the temporal evolution of the NP ejection. Combined measurements of emission and scattering are utilized to examine the dependence of the ablation process on the laser fluence.

Figure 1(a) shows the experimental setup to probe the ablation dynamics. Single shots of the 100 fs laser (Spitfire, Spectra Physics, Inc.) at a wavelength of 800 nm, focused by a 2× objective lens (Mitutoyo), are irradiated onto fresh spots of the silver thin film in a vacuum chamber. We use silver as a target material since its properties and application have been well established.[6,7] Hence, a thin film (~250 nm in thickness) is prepared by electron beam evaporation on

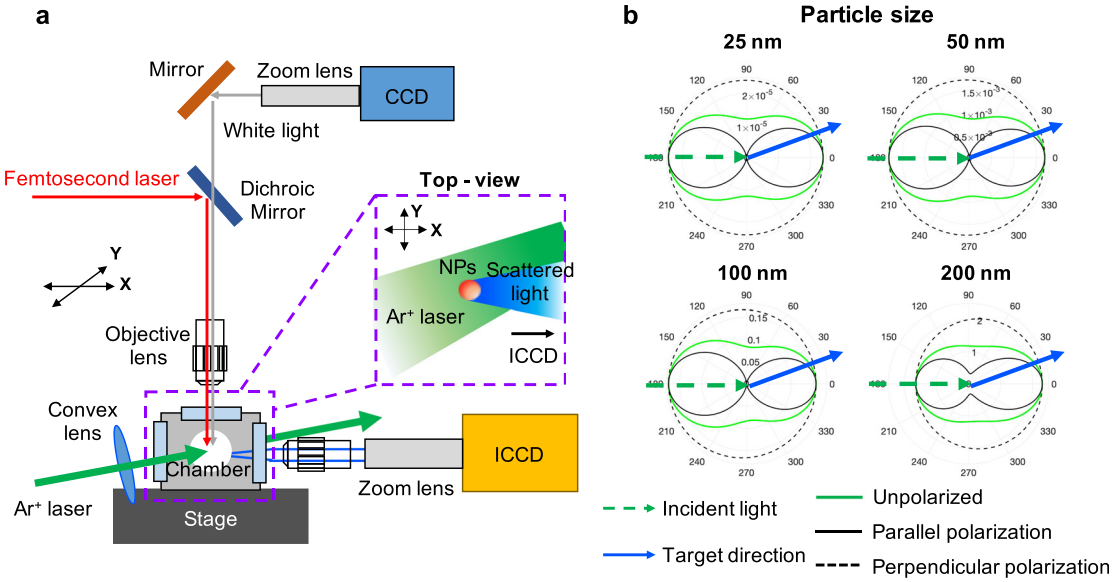

FIG. 1. (a) Optical setup for emission and scattering spectroscopy. The femtosecond laser is irradiated from the top, while emission from the plasma plumes and scattered light from NPs are collected into the ICCD camera. (b) Calculation of angular distribution of scattered light at 514 nm by using Mie theory.

the glass substrate with a 5 nm chromium adhesion layer. To *in situ* probe the plume as well as the formation of NPs, an intensified charge-coupled device (ICCD) camera (PI-MAX, Princeton Instruments) is installed from the side coupled with 5× and 10× objective lenses. Mie theory modeling[15] with complex refractive indices ($n = 0.05$ and $k = 3.26$ at 514 nm) of silver[16] yields the scattering light distributions shown in Fig. 1(b), indicating that forward scattering can cover a wide range of NP sizes. Hence, the probe Ar^+ laser (514 nm) with an optical laser power of 1 W is loosely focused and irradiated from the side at a tilted angle of ∼25°, and the scattered light is collected at 0° to avoid contributions of the directly transmitted probe light.

Figure 2 shows the time-resolved spectrally integrated emission images measured with 5 ns acquisition at different time delays under different pressures, 10^{-5} Torr and 760 Torr. Figure S1 shows the time-resolved spectral emission line spectra. The green line in Fig. 2 represents the target surface of the silver film. Three representative laser fluences are chosen: 1.3 J/cm^2 (just above the ablation threshold ∼1.0 J/cm^2), 2.6 J/cm^2 (near the apparent emission line detection threshold), and 10.5 J/cm^2 (beyond the plasma formation). Detailed analysis regarding the definition of the ablation threshold and the emission detection threshold is discussed in Fig. S2. At 1.3 J/cm^2 near the ablation threshold, spectrally integrated emission is barely seen under both pressures as shown in Fig. 2. On the other hand, as the laser fluence increases to 2.6 J/cm^2 and 10.5 J/cm^2, the intensity of the emission becomes stronger. Up to 5 ns, the expansion proximal to the target surface is similar under both pressures, with the continuum emission[12] dominating the emission spectrum as shown in Fig. S1. After 10 ns, the propagation of the plume is confined as shown in Fig. 2(a) and a shock wave is formed against the ambient atmospheric pressure air of 760 Torr. On the other hand, a conical shaped plume travels freely under 10^{-5} Torr as seen in low magnification images in Fig. 2(b). Moreover, the emission lasts for more than 70 ns under 760 Torr, while its lifetime is shortened to ∼ 70 ns in high vacuum. Under 10^{-5} Torr, the lifetime of the plume is expected to diminish due to reduced collisional events with the background gas molecules.[9] At 1.3 J/cm^2 near the ablation threshold, spectral lines are barely visible in the emission spectrum at both pressures as indicated in Fig. S1. On the other hand, at the fluence of 2.6 J/cm^2, spectral lines of silver neutrals (520.9 nm and 546.5 nm)[17] and chromium neutrals (350–360, 395–400, 425–429, and 520 nm)[18,19] can be detected. At 10.5 J/cm^2, after the initial excitation stage that is accompanied by featureless continuum emission and lasts up to 10 ns, spectral lines of silver and chromium are observable.

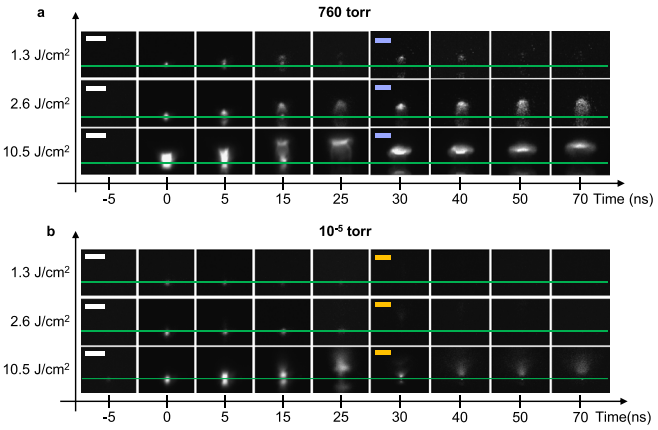

FIG. 2. Spectrally integrated and time-resolved emission spectroscopy measured with 5 ns acquisition under (a) 760 Torr and (b) 10^{-5} Torr. The green line is the target surface plane. Images below the green line are the reflected images by a silver film. The white scale bar is 100 μm, the blue scale bar is 250 μm, and the orange scale bar is 1 mm.

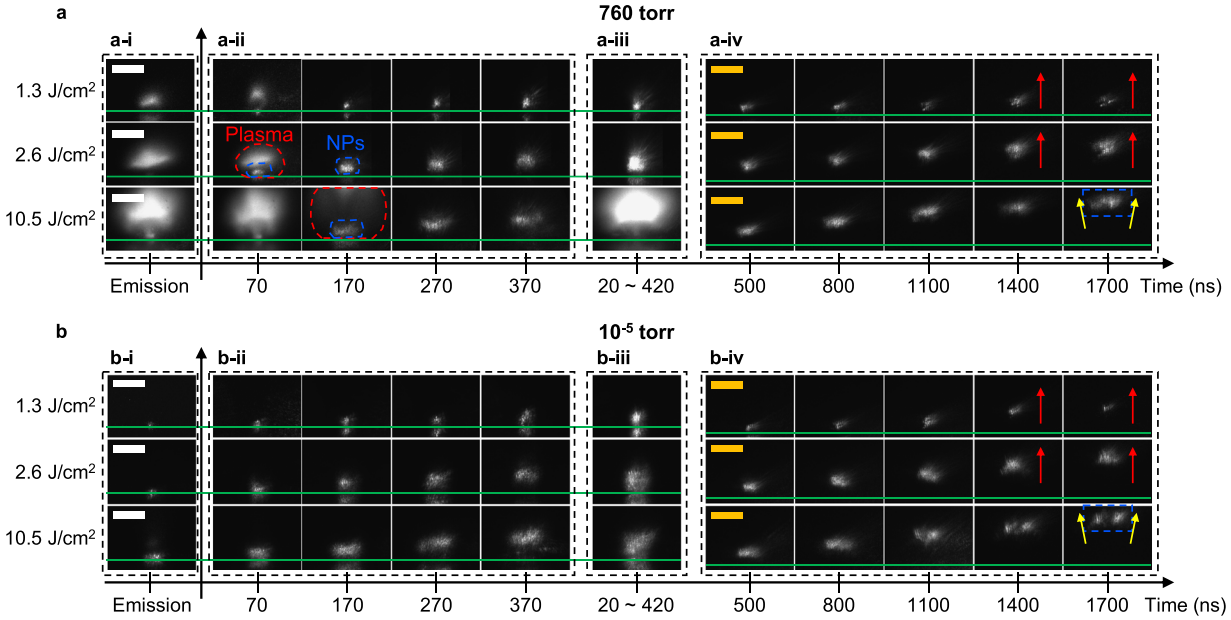

FIG. 3. Time-resolved scattering spectroscopy under (a) 760 Torr and (b) 10^{-5} Torr. The green line indicates the target surface. The images in (a-i) and (b-i) show the emission spectroscopy acquired for 100 ns without probing the Ar^+ laser. Time-resolved scattering images are recorded for (a-ii)–(b-ii) 100 ns, (a-iii)–(b-iii) 400 ns, and (a-iv)–(b-iv) 300 ns acquisition at each time delay. The white scale bar is 100 μm, and the orange scale bar is 200 μm.

Figure 3 shows time-resolved images of Ar^+ laser light scattered off NPs under 10^{-5} Torr and 760 Torr. Images in Figs. 3(a-i) and 3(b-i) are emission measurements obtained for 100 ns acquisition at a time delay of 70 ns without the Ar^+ laser in order to compare with the scattering images. The longer acquisition duration (100 ns) renders the plumes more visible at lower fluences (1.3 J/cm^2 and 2.6 J/cm^2) although they are weak compared to the plume produced at 10.5 J/cm^2, as indicated in the emission measurement in Fig. 2. In the early regime (<500 ns after the irradiation), the ejection of NPs is captured over an acquisition time of 100 ns as shown in Figs. 3(a-ii) and 3(b-ii). Scattering images in Figs. 3(a-iii) and 3(b-iii) are recorded from 20 ns to 420 ns over 400 ns. After a time delay of 500 ns in Figs. 3(a-iv) and 3(b-iv), 300 ns acquisition is used to capture the streaklines of NPs in the large field of view. Figure S3 displays the scattering imaging at the ablation threshold of ~1.0 J/cm^2.

The plumes propagate much faster (3–20 km/s) than the NPs (50–200 m/s) and disappear from the field of view within 170 ns in all cases. In contrast, NPs are still visible at later times. Evidently, the plume affects the direction of the NPs' flight. At 1.3 J/cm^2 and 2.6 J/cm^2, clustered NPs are ejected in the vertical direction (at ~170 m/s at 2.6 J/cm^2 under 10^{-5} Torr), as marked by red arrows at 1400 ns and 1700 ns in Figs. 3(a-iv) and 3(b-iv). Their motion shows that they do not experience significant radial force, even though there is evidence of weak plume ejection. In the case of nanosecond laser ablation, a major contributor is the fluidic transport of the molten pool driven by thermocapillary action in conjunction with the recoil pressure effects. This radial force expels material from the target surface before solidification, resulting in the formation of pronounced rims, large particles (order of micrometers in size), and droplet fingers.[20] In femtosecond laser ablation of thin films, spallation caused by the ultrafast thermodynamic phase change could remove nanometer sized-particle ejecta in the vertical direction with a velocity of ~150–500 m/s. Such speeds were observed by blackbody emission imaging and predicted by molecular dynamic simulations in ultrafast laser ablation of 2–20 nm thick platinum films.[11]

At the fluence of 10.5 J/cm^2, both plume ejection and NP release develop due to the Gaussian variation of the incident local fluence. Plasma formation is expected at the center of the laser beam where the laser fluence is higher than in the peripheral area, which may still experience phase explosion, resulting in the generation of NPs. A distinct difference is the absence of NPs near the center axis at 1700 ns, as shown in Figs. 3(a-iv) and 3(b-iv). We infer that the plume pressure forces the released NP trajectories in the oblique direction as indicated by yellow arrows.

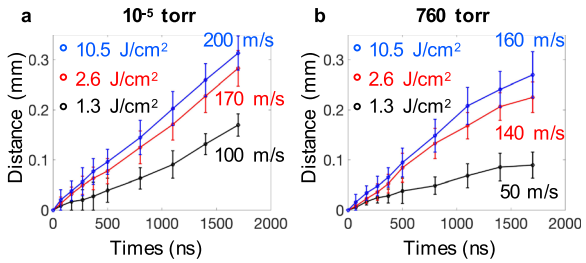

FIG. 4. R–t plot of NPs obtained from scattering spectroscopy under (a) 10^{-5} Torr and (b) 760 Torr. Under 10^{-5} Torr, the R–t curve is linear due to the lack of the background pressure. At 760 Torr, the propagation of NPs is hindered by the atmospheric pressure. The average speeds over 1700 ns are extracted and marked on the plot.

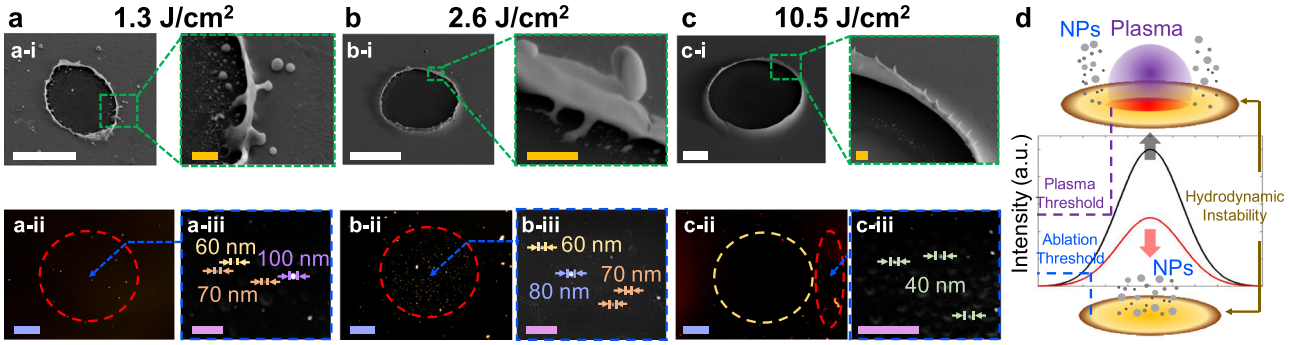

FIG. 5. *Ex situ* characterization of the laser ablated pattern and the collected NPs at different laser fluences: (a) 1.3 J/cm^2, (b) 2.6 J/cm^2, and (c) 10.5 J/cm^2. (a-i)–(c-i) SEM images of ablation features, (a-ii)–(c-ii) DF optical microscope images, (a-iii)–(c-iii) representative SEM images of collected NPs deposited on the receptor substrate within red-circled areas in (a-ii)–(c-ii), and (d) ablation mechanism depending on the laser fluence. The white scale bar is 10 μm, the orange scale bar is 1 μm, the blue scale bar is 100 μm, and the pink scale bar is 500 nm.

Based on acquired images in Fig. 3, the position-delay time (R–t plot) is drawn and the average NP speed is extracted as shown in Fig. 4. Under 10^{-5} Torr, the R–t curves are linear and the maximum NP speed is around 200 m/s at 10.5 J/cm^2, 170 m/s at 2.6 J/cm^2, and 100 m/s at 1.3 J/cm^2. On the other hand, average speeds over a time span of 1700 ns under atmospheric pressure are 160 m/s at 10.5 J/cm^2, 140 m/s at 2.6 J/cm^2, and 50 m/s at 1.3 J/cm^2. In a manner analogous to the plume expansion, drag forces resulting from the ambient atmospheric pressure hinder the propagation of particles.

NPs by single irradiated pulses under 10^{-5} Torr are collected on a receptor glass substrate placed parallel to the target specimen using 500 μm-high spacers. The collected NPs are examined by dark-field (DF) optical microscopy in Figs. 5(a-ii)–5(c-ii), and their sizes measured using scanning electron beam microscope (SEM) images in Figs. 5(a-iii)–5(c-iii). Figure S4 shows the size distribution of collected NPs at each laser fluence. As time resolved scattering images show in Fig. 3, NPs that originate from the spalled layer are chiefly ejected in the vertical direction at 1.3 J/cm^2 and 2.6 J/cm^2 and are, therefore, concentrated right above the irradiated spot as indicated in Figs. 5(a-ii) and 5(b-ii). The sizes of these NPs range from 40 nm up to 100 nm. Particles larger than 100 nm are either re-deposited near the ablated feature or re-solidified at the rim. On the other hand, NPs generated at 10.5 J/cm^2 are sparsely dispersed on the glass substrate and not observable at the center as shown in Fig. 5(c-ii). Considering the time-resolved scattering images in Fig. 3, the absence of NPs at the center is ascribed to the deflection of the NP trajectories by the pressure exerted by the plasma plume. Consequently, at 10.5 J/cm^2, NPs of $\leq$ 45 nm size are observed outside the central area as shown in Fig. 5(c-iii). The thin film ablation mechanism by the femtosecond laser is summarized in Fig. 5(d). All laser fluences, from 1.3 J/cm^2 to 10.5 J/cm^2, leave thorn-types of hydrodynamic instability at the edge of the rim.

In conclusion, we investigated the silver thin film femtosecond laser ablation through time-resolved emission and scattering imaging. The plume and NP ejection processes depend on the applied laser fluence. At high fluences, plumes are emitted from the center area of the irradiated spot and NPs are released from the peripheral area due to the Gaussian laser beam intensity profile. The direction of the NPs is oblique due to the pressure exerted by the ejected plume. At low laser fluences, the NPs are expelled in the vertical direction. Hydrodynamic instability effects yielding thorn-like protrusions are evinced at the elevated rim of the ablated spot. Understanding these mechanisms will help guide the selection of the applied laser fluence at different gas background pressures in order to control the material removal process and improve the machining quality. By conducting spectrally resolved measurements and pushing the resolution to the sub-ns regime, scattering probing can be augmented to analyze the early phase of ablation and also provide quantitative measurements of the NP size and density.

See the supplementary material for time-resolved emission spectroscopy (Fig. S1), the procedure for defining the ablation end emission detection thresholds (Fig. S2), time resolved scattering spectroscopy recorded at an acquisition time of 400 ns at the fluence of 1 J/cm^2 (Fig. S3), and the size distribution of collected nanoparticles (Fig. S4).

This work was done at the Laser Thermal Laboratory, which was supported by Samsung Display through a grant to the University of California, Berkeley.

DATA AVAILABILITY

The data that support the findings of this study are available from the corresponding author upon reasonable request.

REFERENCES

[1]D. Paeng, J. H. Yoo, J. Yeo, D. Lee, E. Kim, S. H. Ko, and C. P. Grigoropoulos, Adv. Mater. **27**, 2762 (2015).
[2]S. Amoruso, N. N. Nedyalkov, X. Wang, G. Ausanio, R. Bruzzese, and P. A. Atanasov, J. Appl. Phys. **110**, 124303 (2011).
[3]B. N. Chichkov, C. Momma, S. Nolte, F. Von Alvensleben, and A. Tünnermann, Appl. Phys. A **63**, 109 (1996).
[4]D. J. Hwang, H. Jeon, C. P. Grigoropoulos, J. Yoo, and R. E. Russo, Appl. Phys. Lett. **91**, 251118 (2007).
[5]C. Kerse, H. Kalaycloğ Lu, P. Elahi, B. Çetin, D. K. Kesim, Ö. Akçaalan, S. Yavaş, M. D. Aşlk, B. Öktem, H. Hoogland, R. Holzwarth, and F. Ö. Ilday, Nature **537**, 84 (2016).
[6]G. Santoro, S. Yu, M. Schwartzkopf, P. Zhang, S. K. Vayalil, J. F. H. Risch, M. A. Rübhausen, M. Hernández, C. Domingo, and S. V. Roth, Appl. Phys. Lett. **104**, 243107 (2014).

[7]A. Shelemin, P. Pleskunov, J. Kousal, J. Drewes, J. Hanuš, S. Ali-Ogly, D. Nikitin, P. Solař, J. Kratochvíl, M. Vaidulych, M. Schwartzkopf, O. Kylián, O. Polonskyi, T. Strunskus, F. Faupel, S. V. Roth, H. Biederman, and A. Choukourov, Part. Part. Syst. Charact. **37**, 1900436 (2020).
[8]K. F. Al-Shboul, S. S. Harilal, and A. Hassanein, J. Appl. Phys. **113**, 163305 (2013).
[9]N. Farid, S. S. Harilal, H. Ding, and A. Hassanein, Appl. Phys. Lett. **103**, 191112 (2013).
[10]C. Wu and L. V. Zhigilei, Appl. Phys. A **114**, 11 (2014).
[11]C. M. Rouleau, C.-Y. Shih, C. Wu, L. V. Zhigilei, A. A. Puretzky, and D. B. Geohegan, Appl. Phys. Lett. **104**, 193106 (2014).
[12]D. Grojo, J. Hermann, and A. Perrone, J. Appl. Phys. **97**, 063306 (2005).
[13]S. Amoruso, R. Bruzzese, N. Spinelli, R. Velotta, M. Vitiello, X. Wang, G. Ausanio, V. Iannotti, and L. Lanotte, Appl. Phys. Lett. **84**, 4502 (2004).
[14]D. G. Papazoglou, A. Karaiskou, I. Zergioti, and C. Fotakis, Appl. Phys. Lett. **81**, 1594 (2002).
[15]C. F. Bohren and D. R. Huffman, *Absorption and Scattering of Light by Small Particles* (Wiley, 1998).
[16]P. B. Johnson and R. W. Christy, Phys. Rev. B **6**, 4370 (1972).
[17]J. C. Pickering and V. Zilio, Eur. Phys. J. D **13**, 181 (2001).
[18]D. J. Hwang, H. Jeon, C. P. Grigoropoulos, J. Yoo, and R. E. Russo, J. Appl. Phys. **104**, 013110 (2008).
[19]W. F. Meggers, C. H. Corliss, and B. F. Scribner, *Table of Spectral-Line Transitions, Part I* (National Bureau of Standards, Washington, DC, 1961).
[20]D. Qi, D. Paeng, J. Yeo, E. Kim, L. Wang, S. Chen, and C. P. Grigoropoulos, Appl. Phys. Lett. **108**, 211602 (2016).